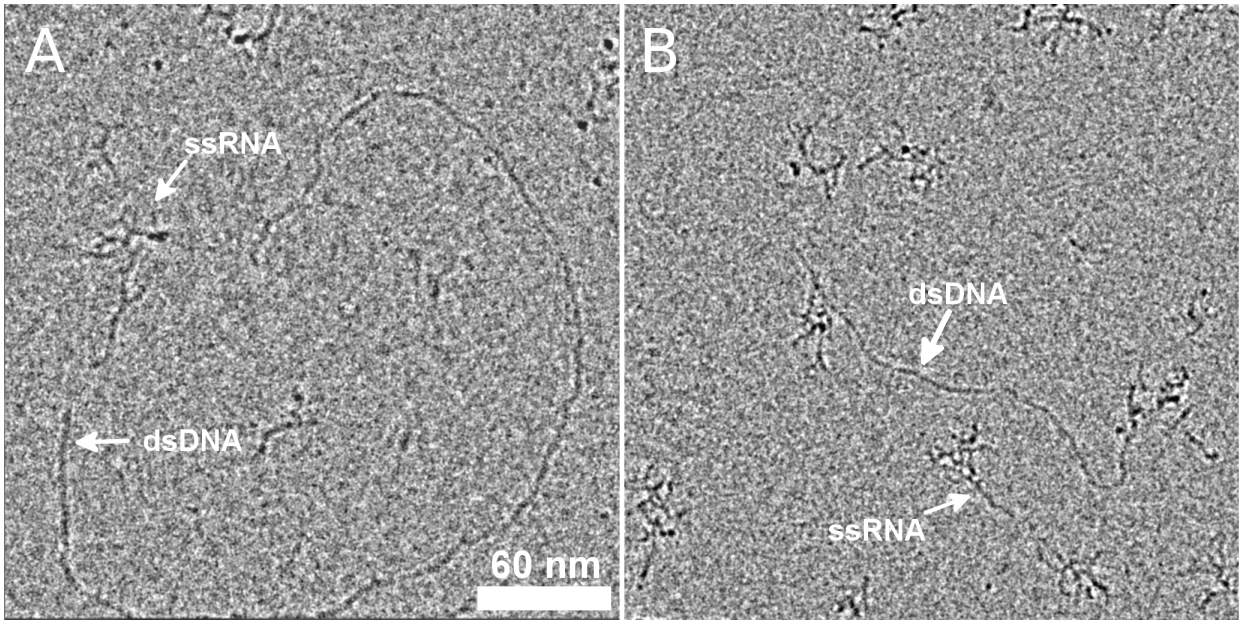

Figure S1: **Comparison of ssRNA and dsDNA by Cryo-EM.** Molecules of a 2117 nt ssRNA imaged in low-ionic-strength TE (Panel A) and physiological Mg^{2+}-containing buffers (Panel B)(see Methods). A small amount of 2141 base-pair dsDNA (transcription template) is added to both samples as internal reference. In each panel it is clear that the widths of the branches seen in ssRNA molecules are comparable to the width of the dsDNA strand. The measured length of the dsDNA molecule in panel A is 662 nm. This value is slightly smaller than the expected 728 nm because undulations of the molecule in the direction of imaging are not accounted for in projections. Only a part of the dsDNA is shown in panel B; it extends to the right beyond the view shown. Branching patterns within ssRNA molecules are easier to discern at low ionic strength (ssRNA arrow in Panel A) because individual arms are distributed farther apart than in physiological buffer (ssRNA arrow in Panel B).

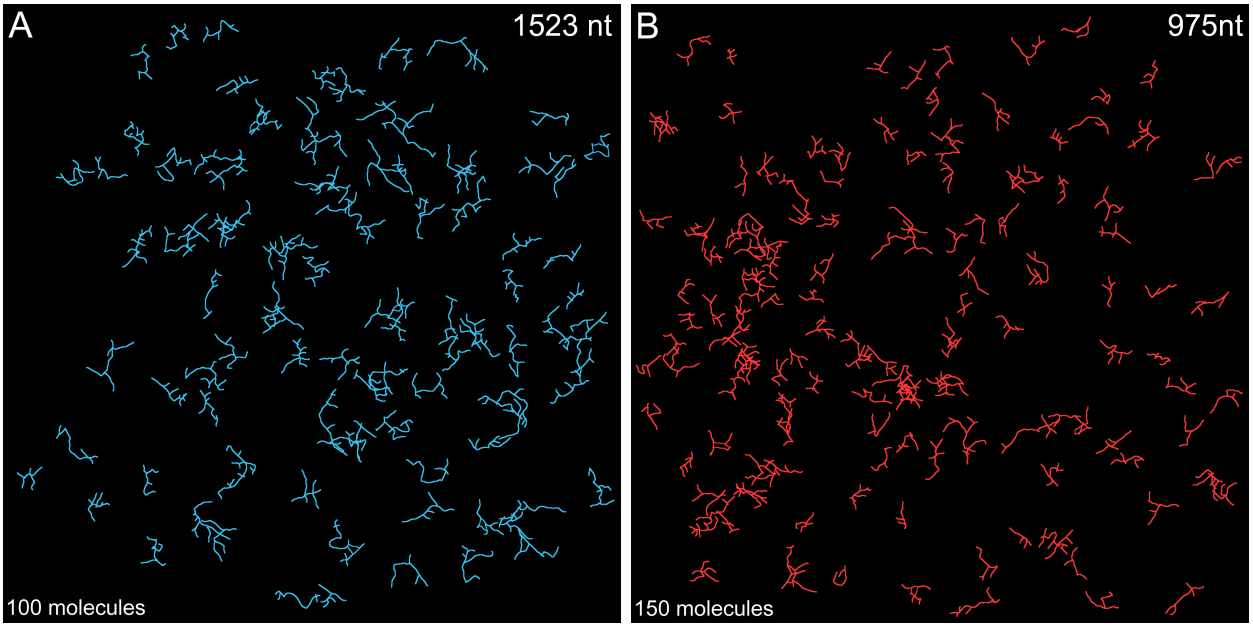

Figure S2: **Additional Molecular Skeletons.** Traced molecular skeletons of RNAs in TE buffer overlaid in the original positions and orientations from the parent image (skeletons from different images may overlap). A) 100 molecules (blue) traced from 12 cryo-EM images of 1523nt RNA. B) 150 molecules (red) of 975nt RNA in TE buffer from 15 cryo-EM images.

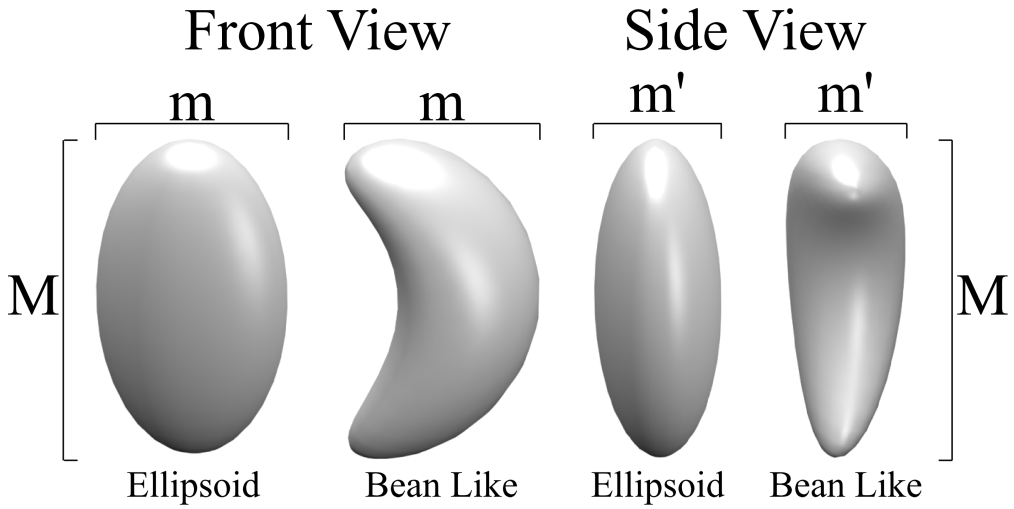

Figure S3: **Comparison of scalene ellipsoids and deformed bean-like prolate models.** Anisotropy determination using Feret diameters cannot distinguish between ellipsoids and other distorted shapes with the same values of M and m for all projections. The anisotropy inferred in Fig. 3 is therefore for an ellipsoid and all equivalent deformed bean-like shapes consistent with the dimensions of the deduced principal axes.

Figure S4: Orthogonal views of MD and SAXS structures, for 1523nt and 975nt RNAs.

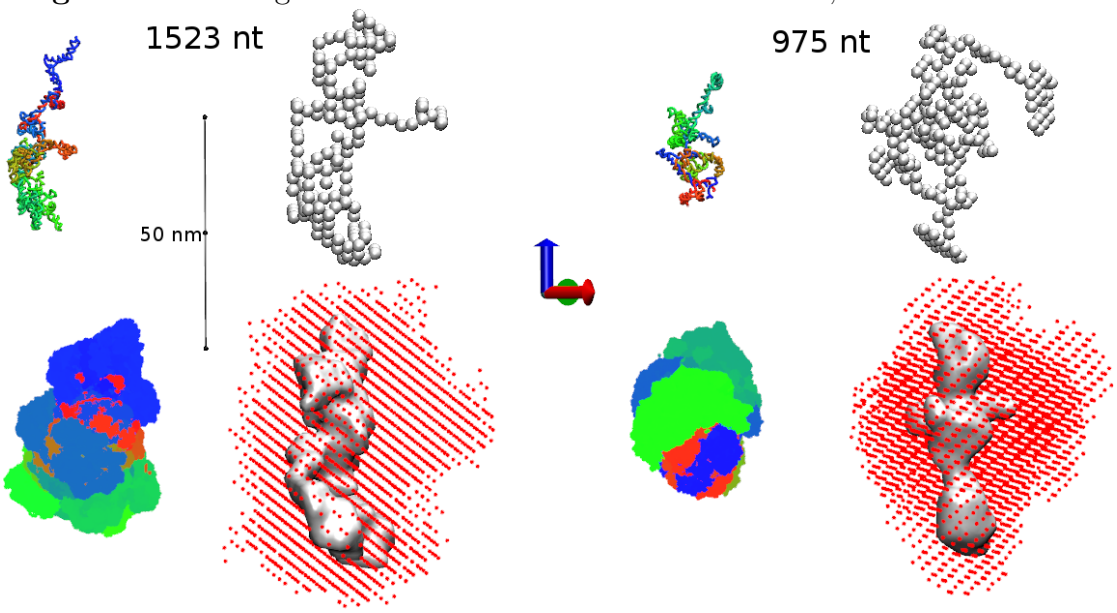

Figure S4A: NAST CGMD models and SAXS reconstructions from Fig. 4 (left: 1523 nt, right: 975 nt) rotated by 90° about the z axis. Notice that the cross-sections from both sets of data are smaller than in Fig. 4, indicating flatness in the molecule.

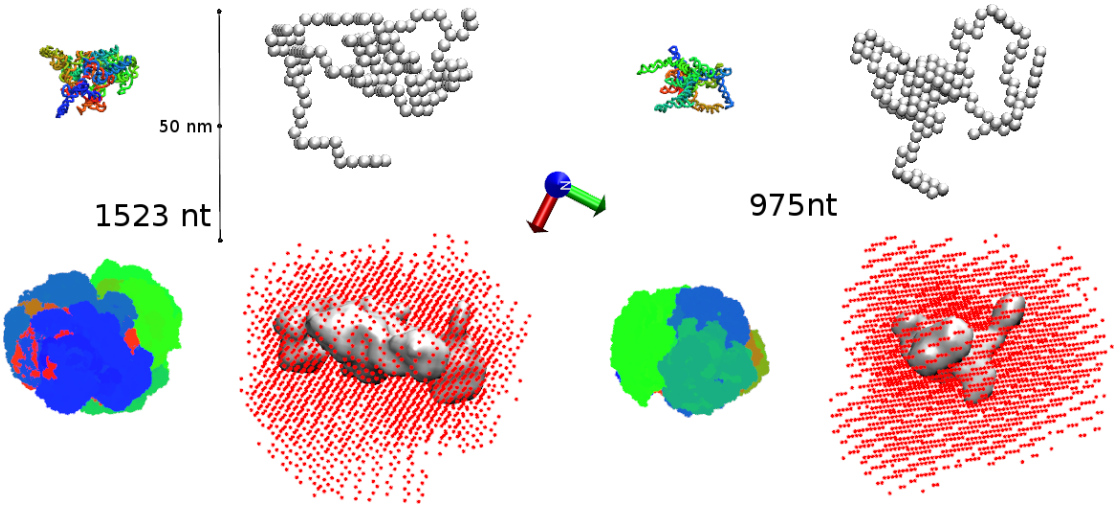

Figure S4B: NAST CGMD models and SAXS reconstructions from Fig. 4 (left: 1523 nt, right: 975 nt) rotated by 90° about the y axis. Notice that the cross-sections from both sets of data are reduced radially, consistent with a prolate shape.

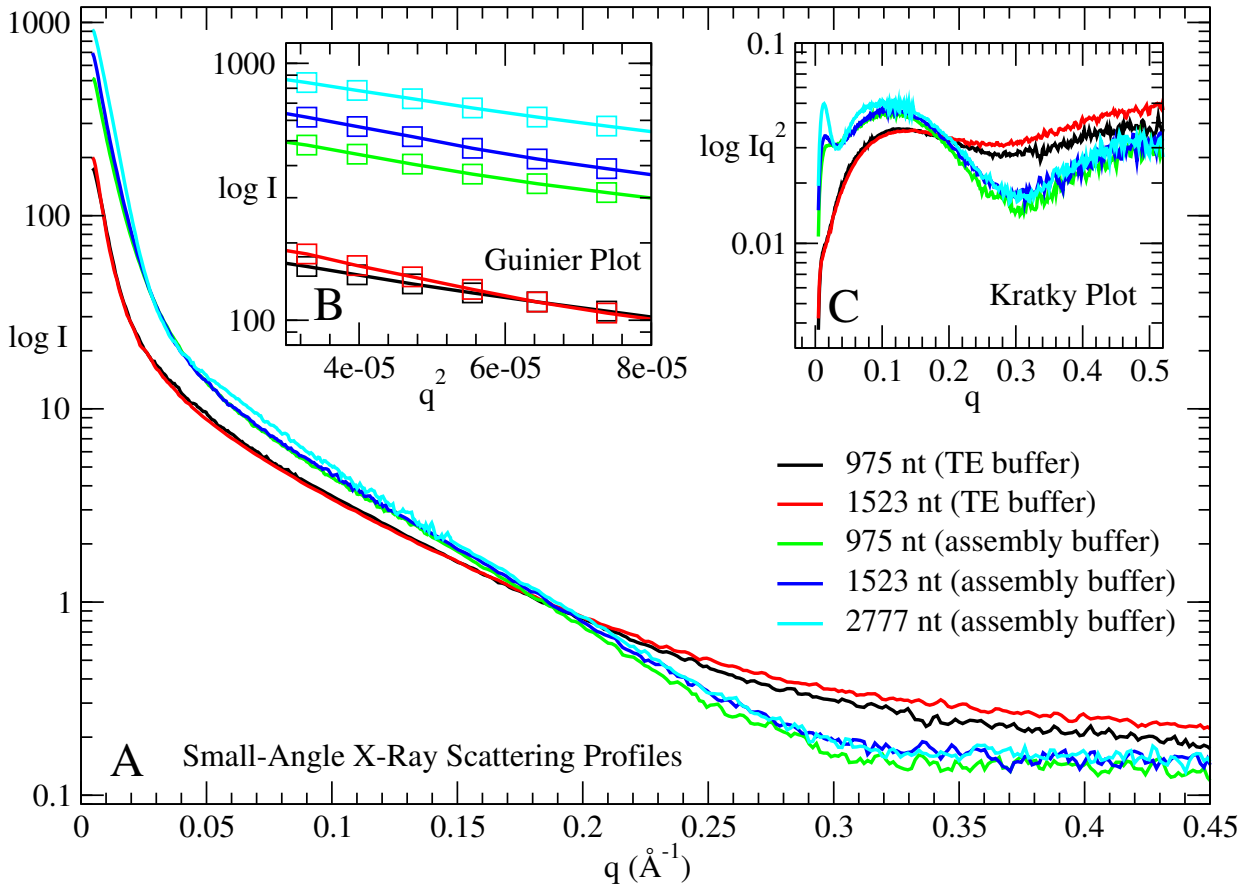

Figure S5: **SAXS Profiles for 975, 1523 and 2777nt RNAs in TE and *in vitro* assembly buffer.** (See Methods). The scattering curves were measured at 1 mg/ml concentration for each RNA. Inset B shows the log I vs. q^2 Guinier plots with linear regions in the qR_g range between 0.7 and 1.3 - corresponding fitted R_gs are shown in Table ST1 below. Measurements were taken at two detector distances and the curves merged to generate the final scattering profile. The higher intensity of the curves for RNAs in *in vitro* assembly buffer (vs. TE) at $0.1 < q < 0.2$ is related to the presence of correlated Mg^{2+} ions. The increased intensity at $q < 0.5$ comes from increased correlations within the condensed RNA molecule. This is easier to visualize in the Kratky plot (inset C) where a distinct peak at $q < 0.05$ Å^{-1} attributable to the overall compactness of the molecule is seen for all three RNA's. The second peak centered around 0.12 Å^{-1} is the signature of double-stranded helical regions.

RNA L [nt]	Buff.	Guinier Fit, PRIMUS R_g [Å]	qR_g	Fid.	From P(r), GNOM R_g [Å]	D_{max} [Å]	QoF	NSD from DAMSUP Avg.(SD)	NAST R_g Avg.(SD) [Å]
975	TE	172±7.5	0.79–1.38	0.99	182	600	0.69	1.80(0.11)	81.0(5.4)
975	IVA	180±2.5	0.83–1.45	0.70	168	550	0.61	1.21(0.27)	⟨77.7(7.6)⟩
1523	TE	199±6.6	0.91–1.60	0.99	208	620	0.62	2.02(0.14)	94.2(6.6)
1523	IVA	188±2.6	0.86–1.51	0.93	206	700	0.75	1.47(0.11)	
2777	IVA	171±2.0	0.88–1.37	0.94	172	600	0.63	1.43(0.12)	124.7(9.1)

Table ST1: RNA Structural Properties from SAXS Data. Fid. = PRIMUS Fidelity Number, QoF = GNOM Goodness of Fit, NSD = Normalized Spatial Discrepancy, IVA = *in vitro* assembly buffer. R_gs calculated from NAST simulations are typically lower than experimental values because they sample compact structures not seen in cryo-EM studies. Ensemble time-averaged NAST R_g from 10 other secondary structures is shown in ⟨ ⟩

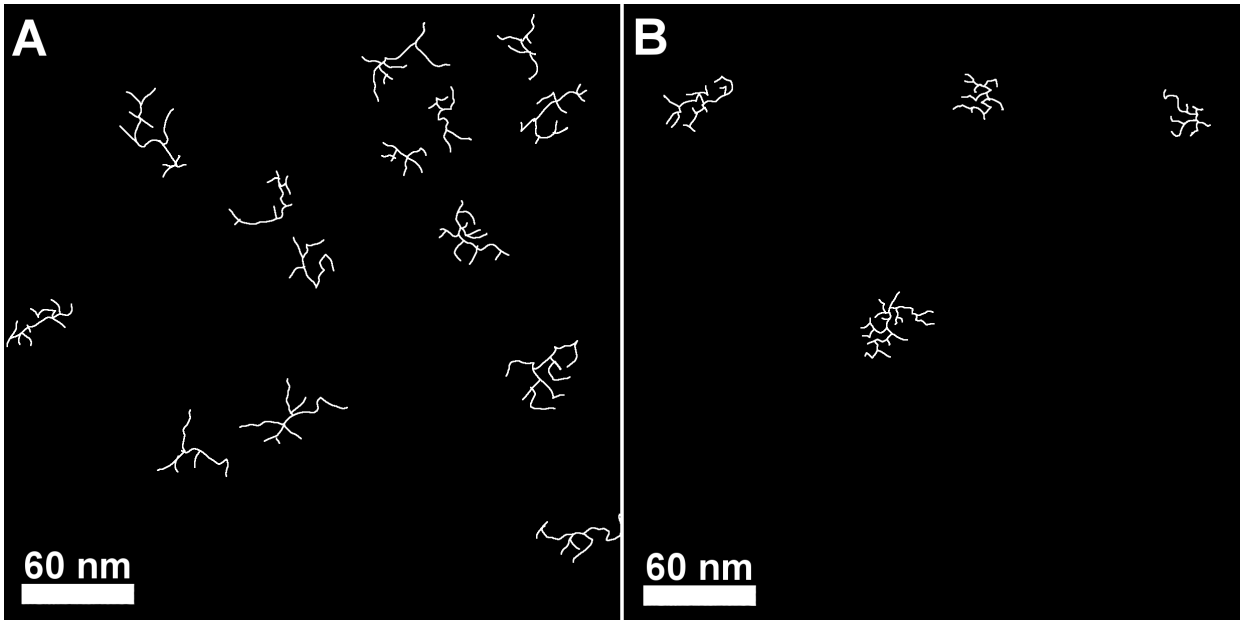

Figure S6: **Traced skeletons of cryo-EM molecular projections of CCMV RNA2 (2777 nt) from Fig. 6 in main text.** Panel A shows projections in TE buffer and Panel B in *in vitro* assembly buffer. The major branched arms in panel A are more extended than in panel B, implying greater rigidity in the former. The total projected area of the molecules in TE is larger than in *in vitro* assembly buffer.

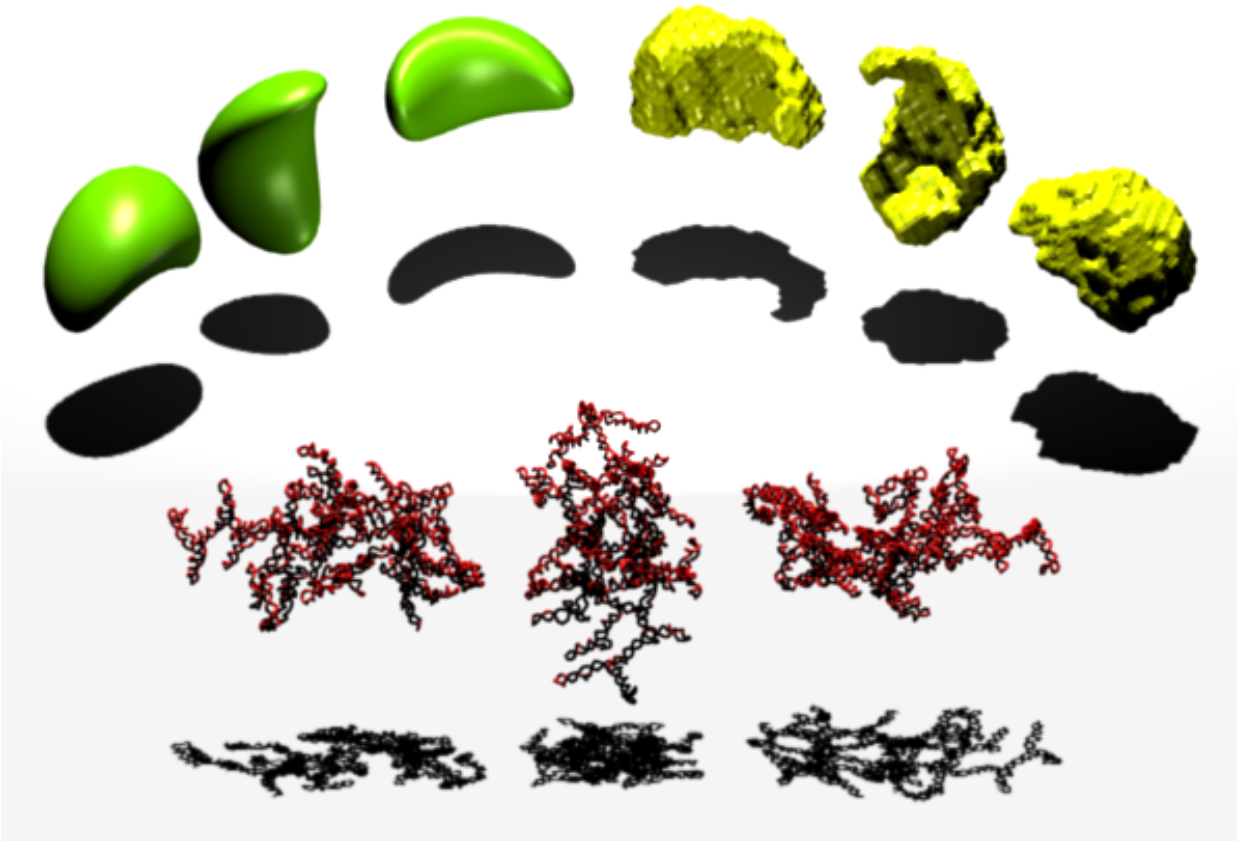

Figure S7: Comparison of orthogonal views and shadow projections of MD structure (red) with the SAXS consensus volume (yellow), for CCMV RNA2. The 3D densities are reconstructed from scattering profiles of the RNA in *in vitro* assembly buffer. The shapes in green are views of a deformed prolate ellipsoid comparable to the SAXS reconstructions.

RNA Length		975nt	1523nt	2777nt
%GC		43.3	41.4	42.5
Avg. Duplex Length including single-base bubbles.		<4.85>	<4.92>	<4.98>
TREE GRAPHS	Total Vertices in Tree Graph	48 <58.8>	77 <92.3>	149 <176.7>
	Terminal Vertices (i.e. stem loops)	20 <19.5>	29 <29.9>	48 <50.0>
	2-fold Junctions	13 <24.7>	22 <38.0>	64 <87.2>
	3-fold Junctions	12 <12.2>	25 <22.1>	30 <33.6>
	4-fold Junctions	3 <2.2>	1 <2.0>	5 <4.6>
	5-fold Junctions	0 <0.2>	0 <0.2>	2 <1.1>
	6-fold Junctions	0 <0>	0 <0>	0 <0.2>
Minimum Free Energy Secondary Structure (longest path highlighted)				

Table ST2: Secondary Structure Properties for 975, 1523 and 2777 nt RNAs. The average duplex length calculation and tree graph calculations are for the minimum free energy (MFE) secondary structures shown in the bottom row and for ensembles of 1000 Boltzmann-sampled secondary structures (ensemble averages values in <>). All secondary structures are predicted using the RNAFold/RNAsubopt programs within the Vienna package (see Methods). Branching analysis is conducted using the RNAs-As-Graphs web application (`http://www.biomath.nyu.edu/rna/analysis/rna_matrix.php`). Diagonal elements of the output Laplacian matrix are used to calculate branching statistics.

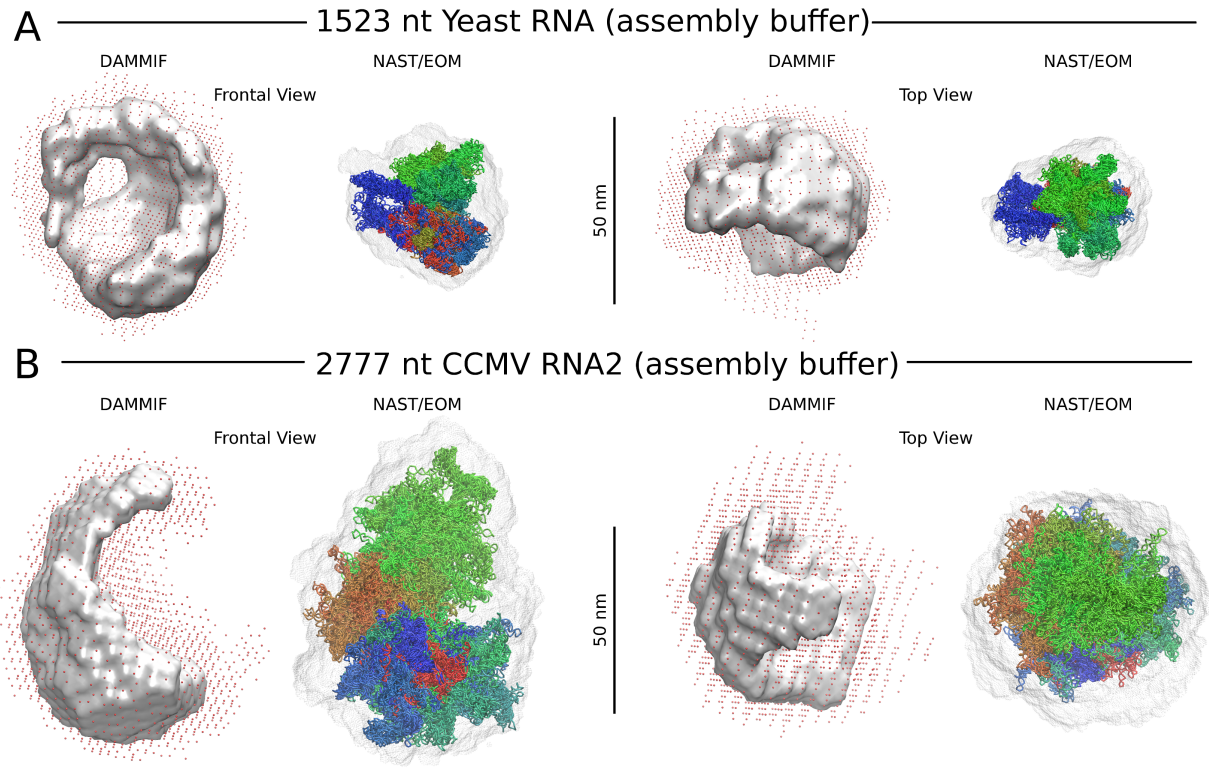

Figure S8: Comparison of SAXS bead reconstructions with EOM optimized NAST CGMD configurations of 1523 (panel A) and 2777 nt RNAs (panel B) in *in vitro* assembly buffer. DAMMIF reconstructed consensus volumes (gray surfaces) are shown within the total volume (red dots) of all superimposed bead structures. The EOM optimized ensembles of NAST configurations (see Methods) are shown as red-green-blue gradient tubes within the total volume of the pool of input configurations (gray dots). Agreement between EOM optimized configurations and SAXS consensus volumes is excellent for the 2777 nt CCMV RNA2, whereas both the dimensions and shape are not accurately determined for the shorter 1523 nt yeast RNA. As mention in the Methods section, this is likely due to the optimized ensemble not reflecting the diversity of secondary structures present in solution.

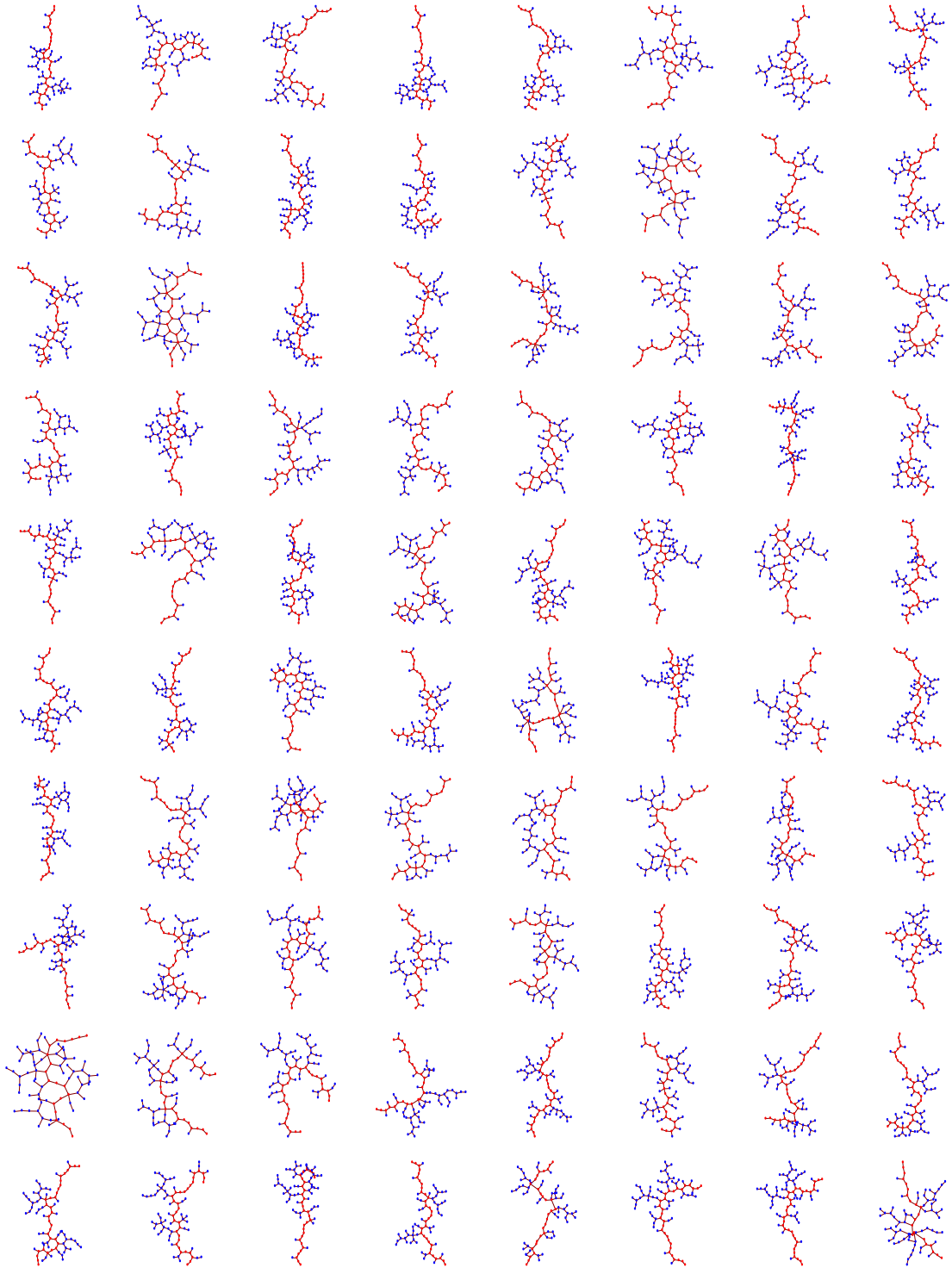

Figure S9: 2D tree-graphs of secondary structures of the 1523 nt RNA. 80 randomly chosen secondary structures from a Boltzmann ensemble of 1000 computed by Vienna are shown. The longest path in each tree is highlighted with red vertices. The trees are not shown to scale (scaling factor between two molecules is the relative lengths of sides). Note that along most maximal paths, there are more vertices of order 2 than 3 or higher.